CrystEngComm

PAPER

Thickness-dependent lattice relaxation and the associated optical properties of ZnO epitaxial films grown on Si (111)

W.-R. Liu,[a] B. H. Lin,[ba] C. C. Kuo,[b] W. C. Lee,[c] M. Hong,[d] J. Kwo,[ef] C.-H. Hsu*[ab] and W. F. Hsieh*[b]

The evolution of the strain state as a function of layer thickness of (0001) oriented ZnO epitaxial films grown by pulsed-laser deposition on Si (111) substrates with a thin oxide Y_2O_3 buffer layer was investigated by high resolution X-ray diffraction (XRD). The ZnO layers experience a tensile strain, which gradually diminishes with increasing layer thickness. Regions with a nearly strain-free lattice develop as the layer thickness exceeds a critical value and are correlated with the emergence of the $<11\bar{2}0>$ oriented crack channels. The influence of the biaxial strain to the vibrational and optical properties of the ZnO layers were also studied by micro-Raman, optical reflectance, and photoluminescence. The deformation-potential parameters, a_λ and b_λ, of the E_2(high) phonon mode are determined to be -740.8 ± 8.4 and -818.5 ± 14.8 cm^{-1}, respectively. The excitonic transitions associated with the FX_A, FX_B, and $D°X_A$ emissions and the A-exciton binding energy all show linear dependence on the in-plane strain with a negative slope.

Introduction

ZnO, a II–VI compound semiconductor, is a promising material for high efficiency light-emitting devices and optical applications for UV luminescence because of its wide direct band gap, 3.37 eV, and large exciton binding energy, 60 meV near 295 K.[1] Because of low cost, excellent quality, large-area availability of Si wafer, and, most importantly, the unique opportunity of integrating well-established Si electronics with ZnO-based optoelectronic devices, many efforts has been involved in growth of high-quality ZnO on Si. Unfortunately, direct growth of epitaxial ZnO films on Si is difficult due to large diversity in lattice constants (15.4%) and thermal expansion coefficient (56%) as well as the formation of amorphous SiO_2 at the ZnO–Si interface.[2] Much effort has therefore been devoted to grow ZnO epitaxial films with the aid of a buffer layer of various materials, such as γ-Al_2O_3, Y_2O_3, Lu_2O_3, Sc_2O_3 and Gd_2O_3 (Ga_2O_3).[3–7] Y_2O_3 has attracted great attention because of its high dielectric constant, high conduction band offset, and thermodynamic stability with Si and is a promising candidate as an alternative gate dielectrics.[8–10] The formation enthalpy of Y_2O_3 is larger in magnitude than that of SiO_2 and ZnO ($\Delta H_{Y_2O_3}$ = -1905.31 kJ mol^{-1}, ΔH_{SiO_2} = -910.7 kJ mol^{-1}, and ΔH_{ZnO} = -350.5 kJ mol^{-1}).[11,12] This implies the formation of an amorphous silica layer at the Y_2O_3–Si interface can be obstructed and provides a nice template for subsequent epitaxial growth. Previous studies showed that ZnO epitaxial films with high crystalline quality can indeed be grown on Si by using a thin Y_2O_3 buffer layer. The lattice of the as-obtained ZnO aligns with the hexagonal O sub-lattice in Y_2O_3 and the interfacial structure can be well described by domain matching epitaxy with 7 or 8 ZnO {11$\bar{2}$0} planes matching 6 or 7 {4$\bar{4}$0} planes of Y_2O_3, leading to a significant reduction of residual strain.[3] The residual strain built up in an *epi*-film, induced by the lattice and thermal mismatches between the overlayer and the substrate, is known to cause a significant modification in its valence-band configuration. Hence, careful characterization of the strain state of a ZnO *epi*-film is pivotal for understanding the influence of strain on its electronic and optical properties and paving the way for the future application of ZnO in photoelectronic devices.

Even though many works reported the strain effects on the electronic and optical properties of ZnO *epi*-layers grown on (0001) oriented sapphire, on which ZnO is compressively stressed,[13] much less is known about the influence on the lattice-dynamical, structural, optical and vibrational properties of the ZnO *epi*-layers on Si, where ZnO is under a tensile strain. In this work, the strain state of the tensile-stressed ZnO *epi*-films was systematically varied as a function of layer thickness in the studied range, 24–1200 nm, and measured by X-ray diffraction. The optical properties of the ZnO films were characterized by optical reflectivity (OR) measurements, photoluminescence at

[a] *Division of Scientific Research, National Synchrotron Radiation Research Center, Hsinchu 30076, Taiwan E-mail: chsu@nsrrc.org.tw; Fax: +886-3-578-3813; Tel: +886-3-578-0281/7118*
[b] *Department of Photonics and Institute of Electro-Optical Engineering National Chiao Tung University, Hsinchu 30010, Taiwan E-mail: wfhsieh@mail.nctu.edu.tw; Fax: +886-3-571-6631; Tel: +886-3-5712121/56316*
[c] *Department of Materials Science & Engineering, National Tsing Hua University, Hsinchu 30013, Taiwan*
[d] *Graduate Institute of Applied Physics and Department of Physics, National Taiwan University, Taipei 10617, Taiwan*
[e] *Center for Condensed Matter Sciences, National Taiwan University, Taipei 10617, Taiwan*
[f] *Department of Physics, National Tsing Hua University, Hsinchu 30013, Taiwan*

low temperature (LT) and micro-Raman spectroscopy accordingly. The phonon deformation-potential parameters, which are linear coefficients describing the phonon frequency shift with residual strain, are also determined.

Experiments

Si (111) wafers were cleaned by the Radio Corporation of America (RCA) method and hydrogen passivated by a buffered hydrofluoric HF acid solution before being put into a multi-chamber MBE/electron-beam evaporation UHV system.[8] A thin Y_2O_3 film was then deposited using electron beam evaporation from a high-purity Y_2O_3 source, with a cubic bixbyite structure of lattice constant $a = 10.606$ Å, on the Si surface, with substrate temperatures maintaining at about 770 °C. The details of the growth conditions and the structure of the Y_2O_3 layer were reported elsewhere.[9,14] The Y_2O_3–Si composite substrates were then transferred in air to a pulsed laser deposition (PLD) growth system. Prior ZnO deposition, Y_2O_3–Si (111) substrates were thermally treated at ~ 375 °C under UHV conditions to clean the surface and to remove the moisture. A beam from a KrF excimer laser ($\lambda = 248$ nm) at a repetition rate of 10 Hz was focused to produce an energy density ~ 5–7 J cm^{-2} on a commercial hot-pressed stoichiometric ZnO (5N) target. Substrate temperature was increased to 400 °C for the successive growth of ZnO layers on the composite substrates without oxygen flow; the growth rate is ~ 0.96 Å s^{-1}.[15]

XRD measurements were performed with a four-circle diffractometer at beamline BL13A of the National Synchrotron Radiation Research Center, Taiwan, with incident wavelength 1.0238 Å. Two pairs of slits located between the sample and the detector yielded a typical resolution of better than 4×10^{-3} Å^{-1}. The samples were also characterized by spatially-resolved Raman scattering using the 488 nm line of an argon ion laser at room temperature (RT). The spot size of the focused laser beam is approximately 1 μm. The scattered light was dispersed by a SPEX 1877C triple spectrograph equipped with a liquid nitrogen-cooled charge-coupled device at 140 K. PL measurements were carried out using a He–Cd laser with a wavelength of 325 nm as the pumping source; a broadband light source (Spex 1682) was utilized for optical reflection (OR) measurements at 13 K. The emitted light was dispersed by a Triax-320 spectrometer and detected by an UV-sensitive photomultiplier tube. The thickness of the thin ZnO films was derived from the period of the Kiessig fringes in X-ray reflectivity curves. For the thick films, the thickness was acquired from the period of interference fringes in room temperature PL spectra and scanning electron microscopy (SEM) cross sectional images.

Results and discussion

Fig. 1 illustrates the XRD θ–2θ radial scan along the surface normal of a 24.6 nm thick sample. The pronounced peaks centered at 2.003 and 2.428 Å^{-1} are Si 111 and ZnO 0002 reflections, respectively; the shoulder at 2.06 Å^{-1} is attributed to Y_2O_3 222 Bragg peak. The presence of the pronounced Kiessig fringes around ZnO 0002 and Y_2O_3 222 reflections reveals the good crystalline quality of the deposited layers and the sharp interfaces between ZnO–Y_2O_3 and Y_2O_3–Si. Two different
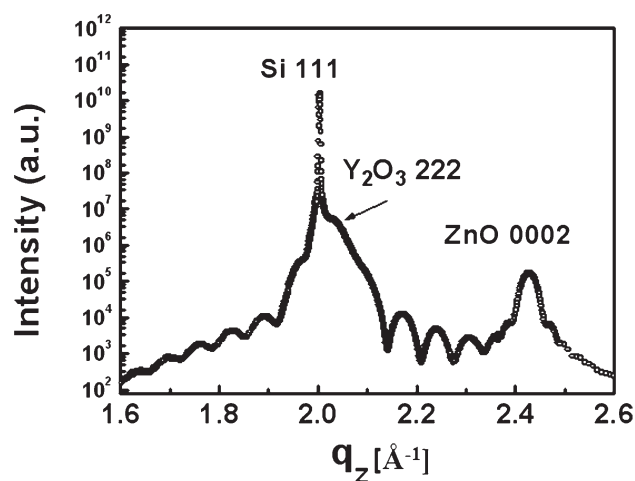

Fig. 1 XRD radial scan along the surface normal of a 24.6 nm thick ZnO layer grown on the Y_2O_3–Si (111) composite substrate.

thicknesses, 24.6 and 9.75 nm, were derived from the fringe periods, which correspond to the ZnO and Y_2O_3 layer, respectively. These numbers are in agreement with the values obtained from X-ray reflectivity. Moreover, the peak width of the ZnO 0002 reflection, 0.02618 Å^{-1}, yields a vertical coherence length of 23.9 nm. This value is close to the ZnO layer thickness, indicating that its structure remains coherent over almost the entire thickness. The intensity profile of the azimuthal ϕ scans across ZnO $10\bar{1}1$, Y_2O_3 440, and Si 220 off-normal reflections are depicted in Fig. 2. Six evenly spaced ZnO $10\bar{1}1$ peaks with their angular positions coinciding with that of the Y_2O_3 440 peaks verify that the hexagonal ZnO film is epitaxially grown on the Y_2O_3–Si (111) substrate. The observation of two sets of Y_2O_3 440 reflections offset by 60° in azimuth are ascribed to the coexistence of two rotational variances of the Y_2O_3 buffer layer. The angular position of the stronger set is rotated with respect to that of the Si 220 by 60°, demonstrating that the Y_2O_3 on Si is predominantly of B-type orientation, i.e., Y_2O_3 {440} ∥ Si {$\bar{1}\bar{1}2$}. The result reveals the relative orientation of the layers follows $(0001) < 2\bar{1}\bar{1}0 >_{ZnO} \| (111) < 10\bar{1} >_{Y_2O_3} \| (111) < 10\bar{1} >_{Si}$.[3] By fitting
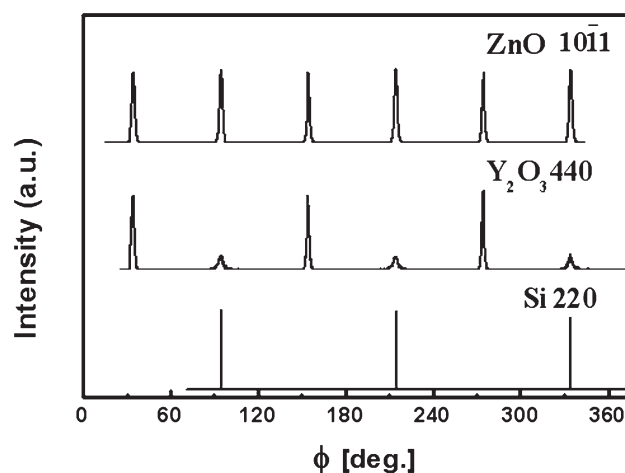

Fig. 2 XRD ϕ scans across ZnO $10\bar{1}1$ and Si 220 off-normal reflections of a 24.6 nm thick ZnO layer.

the angular positions of many Bragg reflections, we determined the lattice parameters of the ZnO layer to be $a = 3.269$ Å and $c = 5.176$ Å. As compared with the bulk values, $a = 3.249$ Å and $c = 5.206$ Å determined from a ZnO wafer, the ZnO epitaxial film was tensily strained (0.64%) in the lateral direction and the lattice along the growth direction is correspondingly compressed by 0.56%.

To probe the strain variation as a function of layer thickness, XRD radial scans along surface normal and $[10\bar{1}0]$ lateral direction were performed on samples of ZnO thickness varying from 24.6 to 1200.5 nm. Fig. 3a and b illustrate, respectively, the profile of the ZnO 0006 normal reflection and $30\bar{3}0$ in-plane reflection. With increasing layer thickness, the center of ZnO 0006 reflection progressively shifts toward smaller normal scattering vector, q_z, and approaches the bulk value, marked by the dashed line in Fig. 3a, indicating the increase of the c-axis lattice constant. Meanwhile, the center of ZnO $30\bar{3}0$ surface reflection exhibits an opposite trend, *i.e.*, increasing with larger thickness, which reveals the relaxation of the tensile strain as the film grows thicker. Besides the relaxation of the homogeneous strain, the peak width of both reflections becomes narrower with increasing thickness, implying the reduction of inhomogeneous strain which is possibly accompanied by increasing structural coherence length. It is noteworthy that an extra peak appears in the radial scans across the $30\bar{3}0$ reflection for samples with ZnO layer thickness of 555.2 nm and above. The circles in Fig. 4a depict the ZnO $30\bar{3}0$ peak profiles of the 555.2 nm thick ZnO layer, which can be nicely decomposed into two Gaussian functions, displayed by dashed curves. The emergence of the extra peak S_R located at a larger lateral scattering vector $q_\parallel = 6.69924$ Å^{-1}, corresponding to a small tensile strain $\varepsilon_{xx} = -0.0011\%$, than that of the original one S_S located at 6.67215 Å^{-1} ($\varepsilon_{xx} = 0.397\%$) reveals the development of regions with a nearly fully relaxed lattice as the film thickness exceeds a

critical value. Carefully examine the peak profile of the specular (0006) reflection of the same sample, shown in Fig. 4b, we observed an asymmetric shape skewing toward the low q_z side. The peak can also be fitted by two Gaussian functions, reflecting the change of the vertical lattice constant in correspondence to the relaxation of lateral lattice constant. The intense one, N_S, centered at high q_z side 7.26885 Å^{-1} is associated with peak S_S in the $30\bar{3}0$ reflection; they are originated from the stressed regions. Alternatively, the weak one, N_R, centered at $q_z = 7.26356$ Å^{-1} with larger vertical lattice constant is associated with peak S_R with smaller lateral lattice constant and they stem from the relaxed regions. As a function of layer thickness, the lateral and normal lattice constants, a and c, of the stressed regions determined by fitting the angular positions of several XRD Bragg reflections, are plotted in Fig. 5a. The lateral/normal lattice constant rapidly decreases/increases with layer thickness in the initial 200 nm and then progressively approaches the bulk value. The corresponding homogeneous strain along the in-plane and surface normal directions, $\varepsilon_{xx} = \dfrac{a - a_0}{a_0}$ and $\varepsilon_{zz} = \dfrac{c - c_0}{c_0}$, where a_0 and c_0 denote the lattice constants of bulk ZnO in the relaxed state, are depicted in Fig. 5b.

The optical microscopy image of the 345.6 nm thick ZnO layer is shown in Fig. 6a, where no crack is found. In contrast, a large density of crack channels running along the ZnO $<11\bar{2}0>$ directions with the $\{10\bar{1}0\}$ side surface are well resolved in the surface image of the 555.2 nm thick ZnO *epi*-layers, shown in Fig. 6b. Apparently, the formation of the crack channels leads to the local relaxation of the tensile strain and accounts for the appearance of extra X-ray diffraction peaks S_R and N_R observed in the thick films. The preferred cracking direction reflects the anisotropic fracture toughness of ZnO. Ding *et al.* reported that the $\{10\bar{1}0\}$ surfaces of wurtzite ZnO had the lowest surface
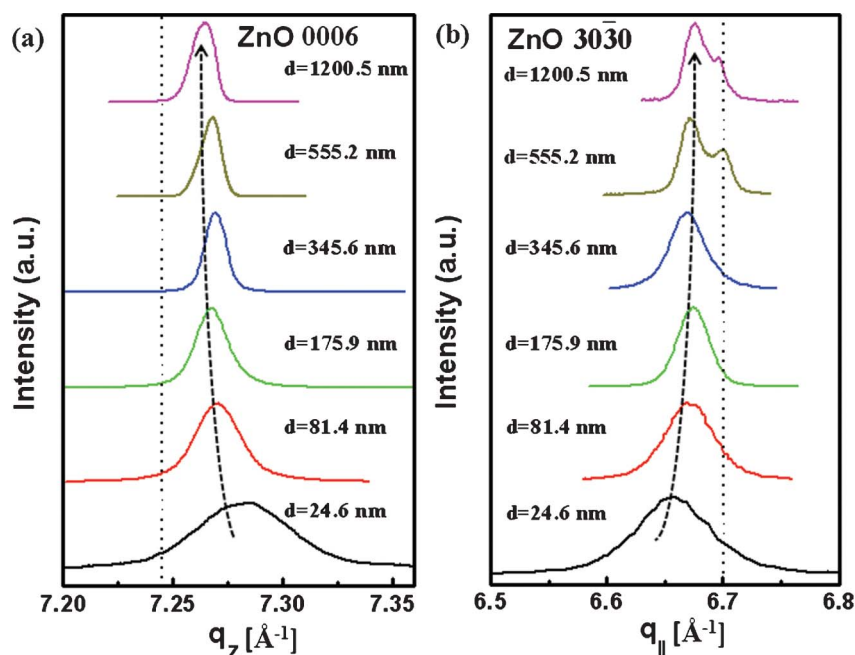

Fig. 3 XRD radial scans across ZnO (a) surface normal 0006 and (b) in-plane $30\bar{3}0$ reflections of six samples with various layer thickness, d. The dashed lines mark the corresponding peak positions of bulk ZnO and the thick dashed curves are plotted to guide the eye.
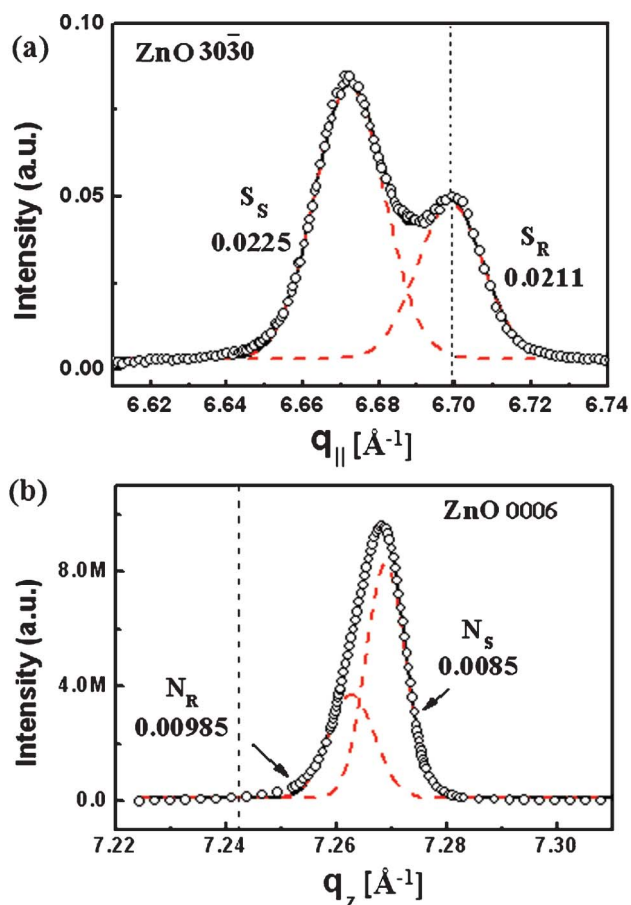
Fig. 4 (a) Peak profile of the in-plane 30$\bar{3}$0 reflection measured with incident angle α_i equal to the critical angle for total external reflection, α_c. The profile is fitted by two Gaussian functions as noted by S_S and S_R. (b) Peak profile of a XRD radial scan across the ZnO 0006 reflection along surface normal, which is fitted by two Gaussian functions as noted by N_R and N_S. All the data were collected from the sample with a 555.2 nm thick ZnO layer. Vertical dashed lines mark the location of corresponding Bragg reflections of a bulk ZnO. The numbers indicated are the corresponding FWHMs.

energy by simple bonding density calculation.[16] The development of the cracks is due to the tensile stress induced by post-growth cooling as a result of the mismatch in the thermal expansion coefficients α_a between ZnO 6.5×10^{-6} K^{-1} and Si 2.6×10^{-6} K^{-1}.[3] Even though Y_2O_3 has a larger thermal expansion coefficient 8.1×10^{-6} K^{-1} than ZnO, it cannot overcome the dictating lattice contraction originating form the Si substrate due to its small thickness.

The crystalline structure of wurtzite ZnO belongs to space group C_{6v}^4 ($P6_3mc$) and has the following optical phonon modes $A_1 + 2B_1 + E_1 + 2E_2$ at the Brillouin zone-center. Among them, the E_2 (high) mode is most sensitive to the strain and often adapted for strain determination.[17] Fig. 7 illustrates the room temperature micro-Raman spectra of the 555.2 nm thick sample recorded in the $z(\ldots)z$ geometry as shown by the schematic inset, where z is parallel to the ZnO c-axis. The spectra were taken with the laser beam focused at three spots with different distances from the cracks as displayed in the inset. Also plotted is the spectrum of a ZnO wafer as a comparison. The residual strain at
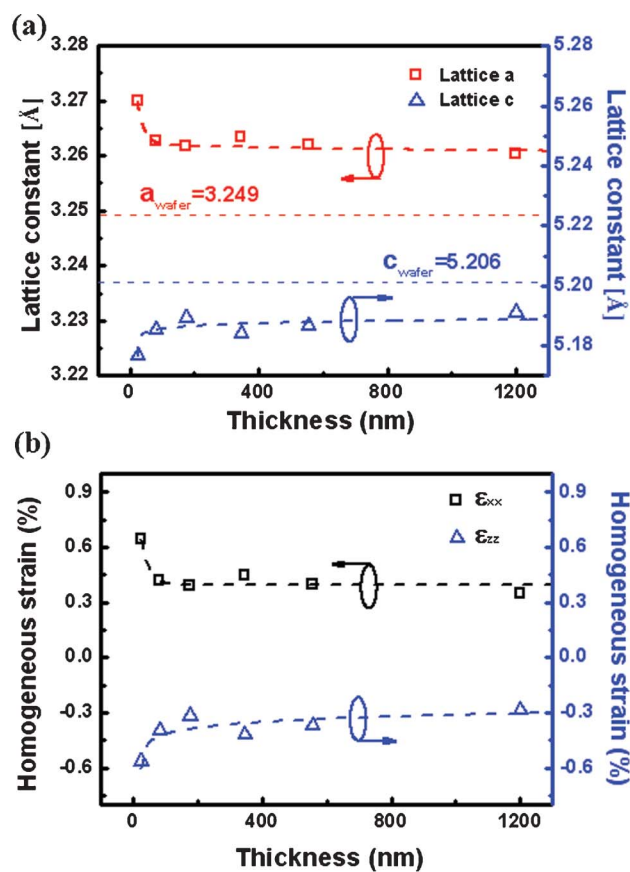

Fig. 5 (a) Lattice constants a and c of the ZnO films as a function of film thickness. The corresponding bulk values are depicted by dashed lines. (b) The homogeneous strain ε_{xx} (in-plane) and ε_{zz} (surface normal) of the ZnO films as a function of the film thickness. The positive values represent the tensile strain. The dashed curves are plotted to guide the eye.
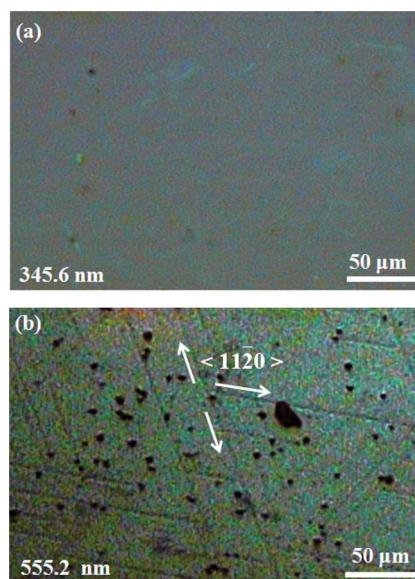

Fig. 6 Optical images of the (a) 345.6 nm and (b) 555.2 nm thick ZnO films grown on Y_2O_3–Si(111) composite substrate.
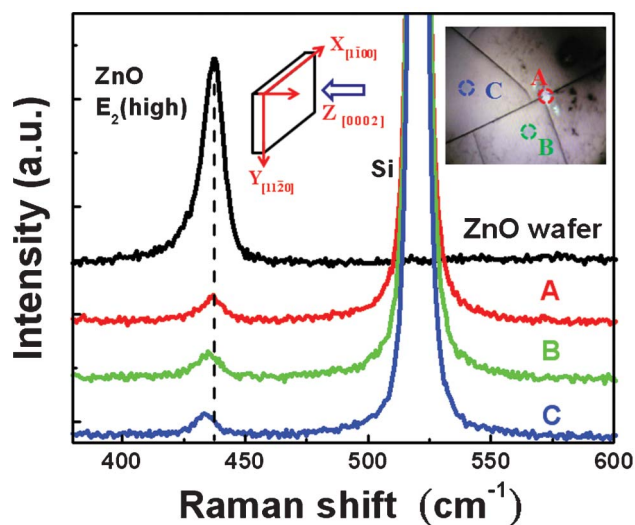
Fig. 7 RT micro-Raman spectra recorded from the 555.2 nm thick ZnO film in the $z(\dots)z$ geometry, as illustrated by the schematic inset. The inset on the upper right corner shows the optical image of the sample surface with the positions of Raman measurements marked.

each location is reflected by the corresponding amount of red shift of the E_2 (high) phonon frequency with respect to that of a strain-free ZnO wafer, 437.78 cm^{-1}. The energy of the E_2 (high) mode measured right on the crack channel, location A, coincides with that of the ZnO wafer, confirming that the local lattice is fully relaxed by the development of the cracks. Moving away from the cracks, the tensile strain gradually builds up as manifested by the increasing red shift observed in locations B and C. Further moving away from the cracks does not cause further red shift of the E_2 (high) frequency. The interior of the regions encircled by the cracking channel are tensily strained and give rise to the XRD peaks S_S and N_S in Fig. 4. Alternatively, the S_r and N_r peaks are associated with the relaxed regions in the immediate vicinity of the cracks.

To quantitatively characterize the influences of stress on optical phonons, the frequency shift of the E_2 (high) mode, $\Delta\omega_\lambda$, was analyzed as a function of lateral strain, ε_{xx}. The micro-Raman spectra, illustrated in Fig. 8a, were recorded in the center of the stressed regions, which is at least 15 μm away from the nearby crack channels,[18] and the E_2 (high) phonon frequency is determined by fitting the Raman peak by a Lorentzian line shape. The strain is deduced from the XRD data and the center of the S_S peak, corresponding to the stressed regions, is adopted. The E_2 (high) phonon mode frequency shift vs. the lateral strain of the ZnO grown on Si with a Y_2O_3 buffer layer (downward triangles) is plotted in Fig. 8b. In addition, the data from the ZnO layers grown under the similar conditions on Si with a nanometer-thick $Gd_2O_3(Ga_2O_3)$, GGO, buffer layer (squares)[7] and on c-plane sapphire (upward triangles), where the ZnO layers are, respectively, under a tensile and compressive strain, are also plotted. In all three systems, the frequency shift exhibits a monotonic dependence on the strain. From the linear least-squares fit to all the data, ranging from compressive to tensile strain, we obtained a slope $m = -665.53 \pm 31.5$ cm^{-1}.

The change in frequency of a phonon mode λ can be described in terms of the phonon deformation potential constants and strain components. Under symmetry conserving stress and in the
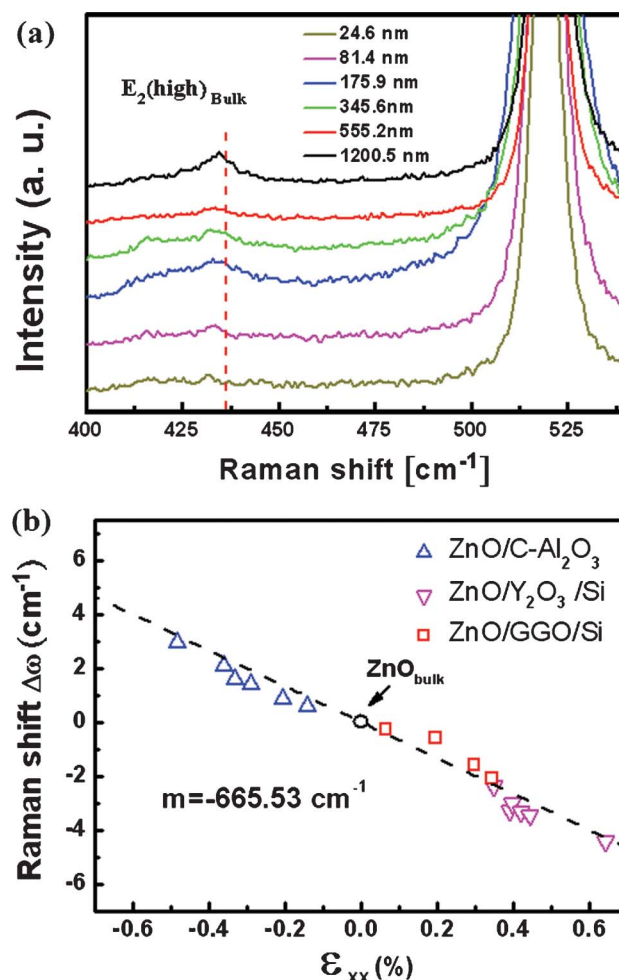

Fig. 8 (a) RT micro-Raman spectra measured in the stressed regions of the ZnO films of different thickness. (b) Frequency shift $\Delta\omega_\lambda$ of the high-energy E_2 phonon mode as a function of lateral strain ε_{xx}. The straight dashed line shows the best linear fit.

linear approximation, the frequency shift $\Delta\omega_\lambda$ of a crystal with C_{6v}^4 ($P6_3mc$) space group symmetry can be expressed by

$$\Delta\omega_\lambda = 2a_\lambda\varepsilon_{xx} + b_\lambda\varepsilon_{zz} \qquad (1)$$

, where the deformation potential constants a_λ and b_λ denote the frequency change of phonon per unit strain along lateral and c-axis directions, respectively.[19,20] This equation holds for the cases of hydrostatic pressure and biaxial strain; where the latter is often caused by lattice mismatch or thermal strain during epitaxial growth.[17] Based on elasticity theory, the strain along the surface normal is proportional to the lateral strain with the ratio $R^b = (\varepsilon_{zz}/\varepsilon_{xx})^b = -2C_{13}/C_{33}$ under the biaxial strain, where C_{ij} denotes the ij component of the elastic stiffness tensor of ZnO.[21,22] Eqn (1) can thus be rewritten as

$$\Delta\omega_\lambda = 2\left(a_\lambda - b_\lambda \frac{C_{13}}{C_{33}}\right)\varepsilon_{xx} \qquad (2)$$

The averaged experimental value of $R^b = -0.92$ is reasonably close to the calculated value -1.00 by adopting $C_{13} = 105.1$ and $C_{33} = 210.9$ GPa reported by T. B. Bateman, indicating the

validity of elasticity theory in the current case.[23] The phonon frequency shift thus varies linearly with the lateral strain. To calculate these deformation potential constants, one more equation is required. The phonon frequency shift under hydrostatic compression and symmetry conserving condition is characterized by the bulk Grüneisen parameter γ, which can be expressed by the deformation potential parameters a_λ and b_λ, the phonon frequency ω_λ under strain-free conditions, and the elastic stiffness constants of ZnO crystal as

$$\gamma = -\frac{2(C_{33}-C_{13})a_\lambda + (C_{11}+C_{12}-2C_{13})b_\lambda}{\omega_\lambda(C_{11}+C_{12}+2C_{33}-4C_{13})} \qquad (3)$$

By inserting the average value for the Grüneisen parameter γ =1.757,[13,24] the E_2 (high) phonon frequency ω_λ = 437.78 cm^{-1}, the elastic stiffness constants at 25 °C, C_{11} = 209.7, C_{12} = 121.1, C_{13} = 105.1, and C_{33} = 210.9 GPa,[23] all with the estimated error of 0.1–0.15%, into eqn (2) and (3), we solve the phonon-deformation potential constants for the E_2 (high) phonon mode to be a_λ = −740.8 ± 8.4 and b_λ = −818.5 ± 14.8 cm^{-1}, respectively. These values are in good agreement with the results a_λ = −690 ± 110 and b_λ = −940 ± 260 cm^{-1} reported by Gruber et al.[13] The discrepancy between the results could be due to the uncertainties in the ZnO Grüneisen parameter and elastic constants used. The defects and unintentional impurity doping may also cause the difference.

The state at the conduction band minimum of ZnO is predominantly s-like (Γ_{7C}). Under the action of crystal-field and spin-orbit interaction, the p-like states in the valence band of wurtzite ZnO are split into 3 levels in the vicinity of the point. The 3 levels at the valence band maximum are commonly labeled as A, B, and C bands in the order of decreasing energy, as shown in the inset of Fig. 9a. Thomas[25] and Hopfield[26] assigned the sequence of p-like valence band in the order of A-Γ_{7V}^u, B-Γ_{9V}, and C-Γ_{7V}^l due to the crystal field and negative spin-orbital splitting. On the contrary, Reynolds[27] and Gil[28] assigned the valence-band ordering as A-Γ_{9V}, B-Γ_{7V}^u, and C-Γ_{7V}^l based on polarized optical reflectance and magneto luminescence measurements on strain-free bulk ZnO crystals. Nevertheless, either ordering predicts that A and B transitions are allowed for light polarization E perpendicular to the c-axis ($E \perp c$), and the C transition is allowed for polarization E parallel to the c-axis ($E \| c$). For many years, the assignment of valence band ordering is still debated and the influence of strain to the electronic structure is of great interest. To access the influence of biaxial strain on the exciton resonance energies of the ZnO epi-film, the optical reflectance (OR) and PL spectra were measured at low temperature. The resonant features in the OR spectrum of the 555.2 nm thick sample, shown in Fig. 9a, with transition energies equal to 3.373, 3.387, and 3.421 eV are attributed to the excitonic transitions associated with the A, B, and C bands, respectively. The B-free exciton (FX$_B$) resonance band is well resolved in all the samples with various thickness; its transition energy is depicted by the circles as a function of in-plane strain ε_{xx} in Fig. 9b. A PL spectrum of the 555.2 nm thick sample in the near-band-edge region is illustrated in Fig. 9a as well. The transitions associated with the A-exciton dominate the LT luminescence; among them the emissions at 3.3604 and 3.373 eV, ascribed to
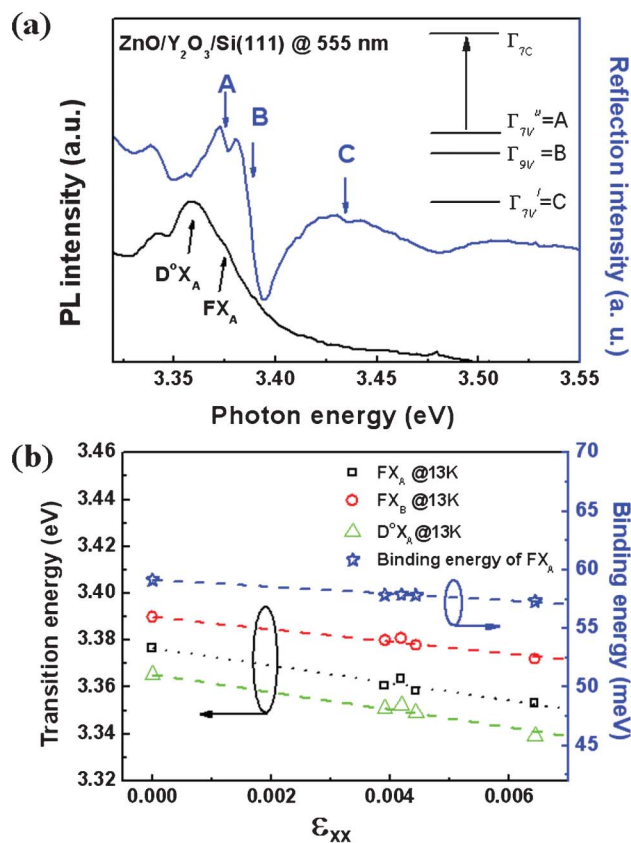

Fig. 9 (a) Optical reflectance and PL spectra of the 555.2 nm thick ZnO epi-layer measured at 13 K. Inset illustrates the ZnO band diagram. (b) Transition energies of FX$_A$, FX$_B$, and D°X$_A$ of ZnO layers measured at 13 K and the binding energy of A exciton as a function of strain, ε_{xx}.

the recombination of A-exciton bound to the neutral donors (D°X$_A$) and the A-free exciton (FX$_A$), respectively, are noted. By fitting the temperature-dependent intensity variation of the FX$_A$ line with the Arrhenius expression,[29,30] we obtained the binding energy of A-exction 58.11 ± 2.4 meV, in good agreement with the 60 meV for bulk ZnO crystal. The transition energies of FX$_A$, D°X$_A$, and the A-exciton binding energy derived from the PL data are also depicted in Fig. 9b as a function of in-plane strain ε_{xx}. The energies of FX$_A$, FX$_B$, and D°X$_A$ exhibit linear dependence on ε_{xx} and the corresponding slopes ($\delta E/\varepsilon_{xx}$) are −3.739, −2.612, and −3.758, respectively. The difference of slopes of FX$_A$ and D°X$_A$ is about 19.3 meV, implying that the binding energy of D°X$_A$ changes at the rate of 19.3 meV with the biaxial strain. According to Hayne's rule, the binding energy of an exciton to a neutral donor–acceptor has a constant ratio to the binding energy of an electron–hole to the donor–acceptor.[31–33] With the reported value 0.3 of Hayne's constant α for ZnO, the variation of localization energy of the donor with strain is calculated to be approximately 64.3 meV.[33–35] The binding energy of the FX$_A$ also exhibits a monotonic decrease with increasing in-plane tensile strain, with a slope of −294.1 meV. This diminishing trend is consistent with the result of the first-principles calculation based on density functional theory with a spatially non-local exchange and correlation functional and spin-orbit interaction.[36] To compare our results with samples grown on different

conditions, we calculate the strain-induced excitonic transition energy shift with respective to the strain along the c-axis ($\delta E/\varepsilon_{zz}$) by taking into account the biaxial strain ratio $R^b = -0.92$ and the values associated with the A and B excitons are 4.06 and 2.84 eV, respectively. These numbers are within in the range with ~ 2 eV for the ZnO grown on c-plane sapphire with and without a layer of GaN buffer layer[13,37] and ~ 15 eV for the ZnO grown on 6H–SiC.[38] The discrepancy may be attributed to the details of the micro-structure, such as defects, and also the difference in strain-free lattice constants adopted.

Summary

Thickness-dependent strain evolution of ZnO epitaxial films grown on Si(111) with a Y_2O_3 buffer layer has been investigated. The ZnO layers are tensily stressed, predominantly due to the difference in thermal expansion coefficient with Si. Drastic strain reduction occurs within the initial 200 nm, attributed to the large density of structural defects in the region near the ZnO–substrate interface as evidenced by the transmission electron microscopy images. Cracking channels develop as the layer thickness exceeds a critical value, less than 550 nm, and leads to the nearly fully relaxed lattice in the immediate vicinity. The interior of the regions encircled by the cracking channels retains a tensile strain of $\sim 0.3\%$. Correlating the peak frequency of micro-Raman spectroscopy with the lattice constants determined by XRD, we found that the energy shift of the strain-sensitive E_2 (high) phonon mode varies linearly with the in-plane biaxial strain. The phonon deformation-potential parameters of the E_2 (high) mode under a biaxial strain model are determined to be $a_\lambda = -740.8 \pm 8.4$ and $b_\lambda = -818.5 \pm 14.8$ cm^{-1}, respectively, in reasonably good agreement with what reported by Gruner et al.[13] PL and OR results reveal that the energy of excitonic transitions of FX_A, FX_B, and $D^\circ X_A$ also exhibit a linear dependence on in-plane strain. A-exciton binding energy also varies linearly with the in-plane tensile strain with a negative slope, which is consistent with theoretic prediction based on the first-principles calculation.

Acknowledgements

References

1 A. Tsukazaki, A. Ohtomo, T. Onuma, M. Ohtani, T. Makino, M. Sumiya, K. Ohtani, S. F. Chichibu, S. Fuke, Y. Segawa, H. Ohno, H. Koinuma and M. Kawasaki, *Nat. Mater.*, 2004, **4**, 42.
2 Y. Z. Yoo, T. Sekiguchi, T. Chikyow, M. Kawasaki, T. Onuma, S. F. Chichibu, J. H. Song and H. Koinuma, *Appl. Phys. Lett.*, 2004, **84**, 502.
3 W.-R. Liu, Y. H. Li, W. F. Hsieh, C.-H. Hsu, W. C. Lee, Y. J. Lee, M. Hong and J. Kwo, *Cryst. Growth Des.*, 2009, **9**, 239.
4 W.-R. Liu, Y. H. Li, W. F. Hsieh, C.-H. Hsu, W. C. Lee, M. Hong and J. Kwo, *J. Phys. D: Appl. Phys.*, 2008, **41**, 065105.
5 W. Guo, A. Allenic, Y. B. Chen, X. Q. Pan, W. Tian, C. Adamo and D. G. Schlom, *Appl. Phys. Lett.*, 2008, **92**, 072101.
6 W. Guo, M. B. Katz, C. T. Nelson, T. Heeg, D. G. Schlom, B. Liu, Y. Che and X. Q. Pan, *Appl. Phys. Lett.*, 2009, **94**, 122107.
7 B. H. Lin, W.-R. Liu, S. Yang, C. C. Kuo, C.-H. Hsu, W. F. Hsieh, W. C. Lee, Y. J. Lee, M. Hong and J. Kwo, *Cryst. Growth Des.*, 2011, **11**, 2846.
8 M. Hong, J. P. Mannaerts, J. E. Bowers, J. Kwo, M. Passlack, W.-Y. Hwang and L. W. Tu, *J. Cryst. Growth*, 1997, **175–176**, 422.
9 C. W. Nieh, Y. J. Lee, W. C. Lee, Z. K. Yang, A. R. Kortan, M. Hong, J. Kwo and C.-H. Hsu, *Appl. Phys. Lett.*, 2008, **92**, 061914.
10 J. Kwo, M. Hong, A. R. Kortan, K. L. Queeney, Y. J. Chabal, J. P. Mannaerts, T. Boone, J. J. Krajewski, A. M. Sergent and J. M. Rosamilia, *Appl. Phys. Lett.*, 2000, **77**, 130.
11 A. Nahhas, H. K. Kim and J. Blachere, *Appl. Phys. Lett.*, 2001, **78**, 1511.
12 J.-J. Liang, A. Navrotsky, T. Ludwig, H. J. Seifert and F. Aldinger, *J. Mater. Res.*, 1999, **14**, 1181.
13 T. Gruber, G. M. Prinz, C. Kirchner, R. Kling, F. Reuss, W. Limmer and A. Waag, *J. Appl. Phys.*, 2004, **96**, 289.
14 Y. J. Lee, W. C. Lee, C. W. Nieh, Z. K. Yang, A. R. Kortan, M. Hong, J. Kwo and C.-H. Hsu, *J. Vac. Sci. Technol., B: Microelectron. Nanometer Struct.–Process., Meas., Phenom.*, 2008, **26**, 1124.
15 W.-R. Liu, W. F. Hsieh, C.-H. Hsu, Keng S. Liang and F. S.-S. Chien, *J. Appl. Crystallogr.*, 2007, **40**, 924.
16 Y. Ding, Z. L. Wang, T. Sun and J. Qiu, *Appl. Phys. Lett.*, 2007, **90**, 153510.
17 J.-M. Wagner and F. Bechstedt, *Phys. Rev. B: Condens. Matter*, 2002, **66**, 115202.
18 S. Tripathy, S. J. Chua, P. Chen and Z. L. Miao, *J. Appl. Phys.*, 2002, **92**, 3503.
19 J. Gleize, M. A. Renucci, J. Frandon, E. Bellet-Amalric and B. Daudin, *J. Appl. Phys.*, 2003, **93**, 2065.
20 J.-Y. Lu, Z.-J. Wang, D.-M. Deng, Y. Wang, K. J. Chen, K.-M. Lau and T.-Y. Zhang, *J. Appl. Phys.*, 2010, **108**, 123520.
21 C. A. Arguello, D. L. Rousseau and S. P. S. Porto, *Phys. Rev.*, 1969, **181**, 1351.
22 F. Decremps, J. Pellicer-Porres, A. M. Saitta, J.-C. Chervin and A. Polian, *Phys. Rev. B: Condens. Matter*, 2002, **65**, 92101.
23 T. B. Bateman, *J. Appl. Phys.*, 1962, **33**, 3309.
24 S. S. Mitra, O. Brafman, W. B. Daniels and R. K. Crawford, *Phys. Rev.*, 1969, **186**, 942.
25 D. G. Thomas, *J. Phys. Chem. Solids*, 1960, **15**, 86.
26 J. J. Hopfield, *J. Phys. Chem. Solids*, 1960, **15**, 97.
27 D. C. Reynolds, D. C. Look, B. Jogai, C. W. Litton, W. Harsch and G. Cantwell, *Phys. Rev. B: Condens. Matter*, 1999, **60**, 2340.
28 B. Gil, *Phys. Rev. B: Condens. Matter*, 2001, **64**, 201310.
29 L. Wang and N. C. Giles, *J. Appl. Phys.*, 2003, **94**, 973.
30 D. S. Jiang, H. Jung and K. J. Ploog, *J. Appl. Phys.*, 1988, **64**, 1371.
31 J. R. Haynes, *Phys. Rev. Lett.*, 1960, **4**, 361.
32 C. F. Klingshirn, *Semiconductor Optics*, Springer, Berlin, 2nd edn. 2005, p. 346.
33 C. F. Klingshirn, B. K. Meyer, A. Waag, A. Hoffmann and J. Geurts, *Zinc Oxide: From Fundamental Properties Towards Novel Applications*, Springer, Berlin, 2010, ch. 7, p. 180.
34 J. J. Hopfield, *Proceedings of the Seventh International Conference Physics of Semiconductors*, Dunod, Paris, 1964, p. 725.
35 D. C. Herbert, *J. Phys. C: Solid State Phys.*, 1977, **10**, 3327.
36 A. Schleife, C. Rödl, F. Fuchs, J. Furthmüller and F. Bechstedt, *Appl. Phys. Lett.*, 2007, **91**, 241915.
37 T. Makino, T. Yasuda, Y. Segawa, A. Ohtomo, K. Tamura, M. Kawasaki and H. Koinuma, *Appl. Phys. Lett.*, 2001, **79**, 1282.
38 A. B. M. A. Ashrafi, B. P. Zhang, N. T. Binh and Y. Segawa, *Appl. Phys. Lett.*, 2004, **84**, 2814.